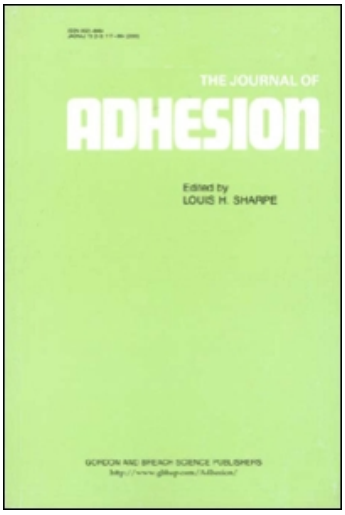

The Journal of Adhesion
Publication details, including instructions for authors and subscription information:
http://www.informaworld.com/smpp/title~content=t713453635

Interfacial Interpretation of Autohesion of Ethylene/1-Octene Copolymers by Atomic Force Microscopy

Hailing Yang[a]; Thomas C. Ward[a]; Wei Zhang[b]
[a] Department of Chemistry, Virginia Tech, Blacksburg, Virginia, USA [b] Advanced and Applied Polymer Processing Institute, Institute for Advanced Learning and Research, Danville, Virginia, USA

To cite this Article Yang, Hailing , Ward, Thomas C. and Zhang, Wei(2007) 'Interfacial Interpretation of Autohesion of Ethylene/1-Octene Copolymers by Atomic Force Microscopy', The Journal of Adhesion, 83: 12, 1043 — 1068
To link to this Article: DOI: 10.1080/00218460701749537
URL: http://dx.doi.org/10.1080/00218460701749537

The Journal of Adhesion, 83:1043–1068, 2007

ISSN: 0021-8464 print/1545-5823 online
DOI: 10.1080/00218460701749537

Taylor & Francis
Taylor & Francis Group

Interfacial Interpretation of Autohesion of Ethylene/1-Octene Copolymers by Atomic Force Microscopy

Hailing Yang
Thomas C. Ward
Department of Chemistry, Virginia Tech, Blacksburg, Virginia, USA

Wei Zhang
Advanced and Applied Polymer Processing Institute, Institute for Advanced Learning and Research, Danville, Virginia, USA

The T-peel fractured surfaces of bonded films of ethylene/1-octene copolymers with different 1-octene contents were characterized using atomic force microscopy (AFM) and analyzed by fractal analysis. The AFM images showed strong dependence on the bonding temperature, peel rate, and the 1-octene content visually. This dependence has been demonstrated quantitatively by the fractal analyses which quantified an irregular surface by fractal dimensions and characteristic sizes. Two regimes showing fractal features were identified for each surface. In Regime I (higher magnifications) the welding and the following T-peel fracture procedures did little to change the fractal dimensions compared with the original surfaces before welding. But there were significant changes in Regime II (lower magnification) before welding and after T-peel fracture tests. The length scale that separated these two regimes is of the same order as that of polyethylene lamellar crystal structures. This suggests that the amorphous chains interdiffused across the interface while unmelted interfacial crystal structures remain essentially unaltered during the autohesion process. A "stitch-welding" autohesion mechanism was proposed to describe the bonding process in which only chains in the amorphous portions could interdiffuse. During the T-peel fracture tests, a crystal structure on the interface is either pulled over to the other side of the interface due to the interdiffused chains, remains unchanged, or is used as an anchor to pull a crystal structure from the other side of the interface. The characteristic sizes at which the fractal characteristics emerge were shown to be larger for the surfaces fractured at higher peel rates, which corresponds to higher fracture energy. This suggests that the appearance of fractal behavior at larger scales requires higher fracture energies. The characteristic sizes and fractal dimensions were also shown to depend on the molecular structure.

Received 25 January 2007; in final form 4 October 2007.
Address correspondence to Hailing Yang, Institute for Advanced Learning and Research, 150 Slayton Ave., Danville, VA, 24540, USA. E-mail: hayang@vt.edu

Keywords: Atomic force microscopy (AFM); Ethylene/1-octene copolymers; Fractal dimension; Fractals; Peel energy; Stitch-welding; Symmetric interfaces

INTRODUCTION

Polymer welding is a common process encountered in polymer processing and is usually generated between two surfaces of polymers [1]. Autohesion is defined as the resistance to the separation of a bonded interface of two identical polymers [2]. Studies on the autohesion phenomenon can provide fundamental insights into the chain dynamics and thermodynamics as well as the practical engineering issues such as crack healing, elastomer tack, polymer fusion, self-healing, and polymer welding. This information may help product and process design because the interfacial structures can play a critical role in determining final properties, reliability, and the function of polymeric materials.

A full understanding of the autohesion process of polymers such as the ethylene/1-octene (EO) copolymers involves investigations at three different length scales [1,3]: 1) a molecular scale which controls the interfacial structure; 2) a mesoscopic or microscopic scale which can provide information to describe how the energy is dissipated during a fracture process; and 3) a macroscopic scale at which mechanical properties such as fracture energy can be obtained for a particular test geometry [4–5]. Recently, the availability of surface analysis techniques such as scanning probe microscopy and of polymers with controlled molecular structures has provided a better understanding of the molecular structure at polymer interfaces. This acquired knowledge is very useful for correlating the interfacial structure and its ability to sustain a measurable crack growth energy at the interface of polyethylenes, especially when short hexyl branches are introduced into the chain topologies.

Atomic force microscopy (AFM) is a powerful tool to investigate the fractured surfaces in the mesoscopic and microscopic scales by mapping the topography of these surfaces [6–7]. The topography features of these surfaces can be used for better understanding of the deformation process at the interfaces leading to failure. It is usually more useful if such information can be quantitatively extracted from the AFM images and to correlate with the macroscopic scale parameters, such as fracture toughness. Root-mean-square (RMS) roughness (R_q) is the most reported parameter obtained by compiling the various moments of the height distribution of an AFM image.

However, it is insufficient to provide the information on the surface orientation or dimensionality [8]. Power spectral density (PSD) is a better way than the RMS roughness to quantitatively characterize the surface roughness. It transforms the AFM spatial elements into an array of time-dependent constructs (sine waves) using fast Fourier transformation. It is used to determine the most probable underlying wavelength, which may reflect the dominant physical features of the surface's topography [9]. However, the limitation is that PSD only reveals the periodic surface features since this approach characterizes by a series of fixed wavelengths or frequencies. Therefore, PSD is much more useful in analyzing a uniform, flat or regular patterned surface rather than complex, irregular geometry, such as fractured surfaces.

A disordered surface may be described better by fractal analysis because disorderliness is the intrinsic feature of the fractal concept. The concepts of fractal geometry were pioneered by Mandelbrot in his book [10]. Fractals are disordered systems that can be described in terms of non-integral dimensions [11]. One of the remarkable features of fractal geometry is that it is a powerful tool in which simple rules can be applied to build up realistically complex objects, whereas conventional Euclidean geometry does not actually describe the objects found in nature just by drawing straight lines and/or circular arcs [12]. Fractal geometry also treats the disorder as an intrinsic property rather than as a perturbative phenomenon. Furthermore, fractal dimensions can be related to physical processes or mechanisms that operate to produce real objects and surfaces [13]. Fractal dimension, D, calculated from fractal geometry, can represent the height irregularity of the examined surfaces quantitatively. Therefore, the quantitative comparisons between complex surfaces become much easier and more precise. The fractal dimension can be directly related to the irregularity of a surface. Some previous investigations have shown that a higher fractal dimension correlates to a more geometrically complex surface [14–15].

The fractal analysis of this work uses a continuum model to compute the dimensionality of these surfaces [16]. Ideally, a fractal surface was mathematically defined as having a statistical self-similarity at *any* dimension scale. However, many real fractured surfaces were observed to have fractal features only over a *limited* range of scale. The cell sizes described in this article at which the fractal characteristics emerge, or fractal dimension changes, are defined as the characteristic sizes. The characteristic sizes may also describe the fractals quantitatively because they account for the scale at which the self-similarity appears, or the dominant pattern changes.

EO copolymers, which are branched polyethylenes and are usually called linear low density polyethylenes (LLDPEs), are one of the major classes of semicrystalline polymers. Formation of adhesion bonds between these materials is typically useful for package sealing, among other important applications [16–17]. In this work, fractal analysis of the surface topography of EO copolymers both before bonding and after T-peel fracture testing is discussed. The fractured surfaces obtained in autohesion of branched polyethylenes do not consist of either 100% amorphous structure or of a single homogeneous crystal [18]. There are either two or more distinct phases with different crystal structure and composition, or many grains with essentially random orientation. It is reasonable to suppose that these differences, which affect mechanical and physical properties, might change the fractal characteristics and, consequently, the local fractal dimension [19–20]. This information from fractal analysis, in return, will help the understanding of the structure-property relationships of these materials.

EXPERIMENTAL

1. Materials

The three polyethylene samples used in this study include an HDPE (EO-1) and two EO copolymers (EO-2, EO-3) (Dow® Chemical Company, Freeport, TX). The 1-octene contents are 0.00, 4.30, and 7.80 wt%, respectively. Gel permeation chromatography (GPC) results show that their molecular weights and molecular weight distributions are quite similar. Differential scanning calorimetry (DSC) shows that the crystallinity decreases with increasing the branching degree. The available molecular characteristics of these samples are listed in Table 1.

TABLE 1 Molecular Characteristic of Ethylene/1-Octene Copolymers

PE sample	EO-1	EO-2	EO-3
1-octene wt%	0.00	4.30	7.80
1-octene mol%	0.00	1.11	2.07
Density, g/cm^3	0.952	0.935	0.927
Melt index (I_2)	3.81	2.55	1.95
M_n (GPC)	22200	23700	24400
PDI (M_w/M_n)	3.65	3.90	3.93
M_z (GPC)	229600	274200	283700
Degree of branching/1000C	0.00	5.38	9.75
Crystallinity, %	73	62	58

2. METHODOLOGY

2.1. Molding Films

Molding of the HDPE and the two EO copolymer films was done by "melt-pressing" the pellets by using a Tetrahedron® Smartpress Compression Molding Instrument (Tetrahedron Assoc., San Diego, CA) between two Kapton® (500 μm) films covered by two stainless steel sheets at 193°C and 182°C, respectively, for 8 minutes using a pressure about 3.36 MPa and degassing by 3 time bump cycles (*i.e.*, controlled opening and closing of the press to prevent or reduce formation of air bubbles in the film). The films were then cooled to room temperature at 10°C/min.

2.2. Bonding Films

The experimental setup for strip bonding is shown in Figure 1. The molded films were cut into strips with dimension of 0.5 mm in thickness, 20 mm in width, and 120 mm in length. Two of these strips of the same polymer were bonded at a number of bonding temperatures (T_b) by applying a pressure at about 1.13 MPa for several bonding times using the Tetrahedron® Smartpress Compression Molding Instrument. The bonded strips were then cooled down to room temperature at a controlled cooling rate of 10°C/min. The bonding temperatures were chosen at 120°C and 130°C for 1 hour of bonding time. The variations in the actual bonding temperatures were monitored by an Omega® 20 μm-thick copper-constantan type-T thermocouple probe with precision of ±0.5°C [21] (Omega Engineering, Stanford CT).

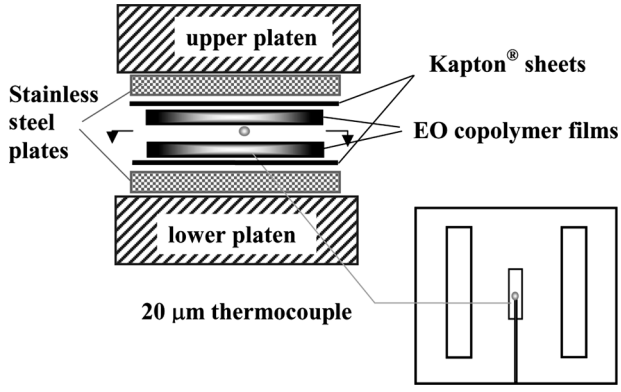

FIGURE 1 Schematic of bonding process.

The thermocouple was inserted into the two molded films using an extra pair of strips to avoid interference to the specimens for further testing.

2.3. Differential Scanning Calorimetry (DSC)

The thermal behavior of each molded EO copolymer film was characterized using a differential scanning calorimeter (TA MDSC 2902, Thermal Analysis Instruments®, Wilmington, DE). Experiments were performed at different scanning rates ranging from 5 to 20°C/min. The characteristic temperature (defined in Sec. 1 under Results and Data Analyses) was determined from DSC measurements with different heating rates. Temperature calibration of the DSC during heating was accomplished by recording the onset of the melting transition of an indium standard sandwiched between two molded branched polyethylene films. Temperature calibration during cooling was achieved by recording the isotropic-to-nematic transition of p-azoxyanisole ($T_{I\text{-}N} = 136$°C). The ΔT reveals the difference in the bonding temperature and the characteristic temperature [22].

2.4. T-Peel Fracture Testing

The peel energies (G_{1c}) of the symmetrically bonded polyethylene films were determined by T-peel fracture tests according to the ASTM standard method D1876-01 [23]. The T-peel test is a method for determination of the adhesive fracture strength and fracture energy. In steady state, a bonded sample with two laminates of width b, and a thickness h are peeled at peel force, F, as shown in Figure 2. At a peeling displacement, ℓ, the crack has advanced over a distance, a. The elongation in the arms is always small; therefore, $\ell = 2a$. In this study, the peel energy, G_{1c}, is defined as the energy to separate the bonded sample per unit area [24]

$$G_{1c} = \frac{1}{ab}\int_0^{\ell} F d\ell = \frac{2F}{b} \tag{1}$$

and the peel strength, P, according to ASTM D1876-01, is defined as

$$P = \frac{F}{b}. \tag{2}$$

Note that the units for peel energy and peel strength do not fit the classical definition here. The Instron 5500 tensile testing instrument (Instron, Northwood, MA) was used to record the applied force as a function of displacement and time. All the T-peel tests were performed

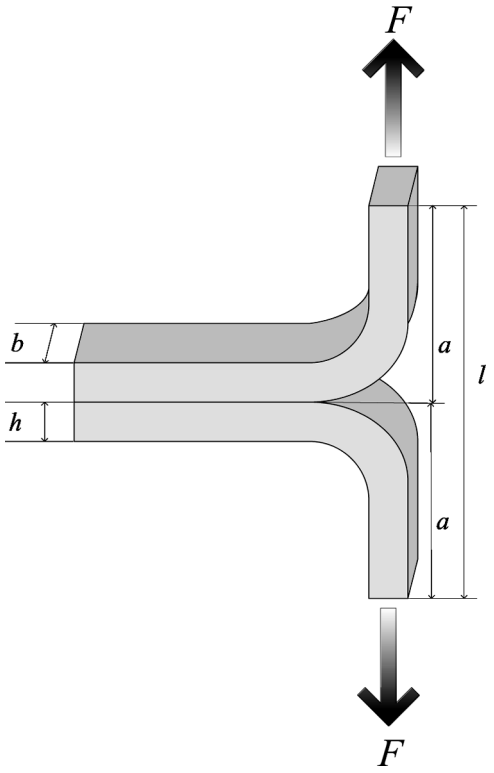

FIGURE 2 T-peel geometry.

at room temperature (23–25°C). The peel rate was preset at three different values: 2, 20, and 200 mm/min. All G_{1c} values that will be discussed in this work are the average values of at least three measurements.

2.5. Atomic Force Microscopy (AFM) Characterization of Surfaces

The surface morphology and topology study of polymer films before bonding and also after T-peel fracture tests was carried out using a Digital Instrument® Dimension 3000 atomic force microscope (Veeco, Santa Barbara, CA). The AFM was operated in tapping mode at room temperature using nanosensor tapping etched silicon probes (TESP) type single beam cantilevers. The amplitudes of the drive signal used to set the cantilever oscillation were in the range between 2.8 and 4.2 V. The scan rate ranges from 0.8 to 1 Hz. The images were

processed only by flattening to remove background shapes. Images were collected in both the height and phase modes.

Fractal analyses of the AFM results were performed using the fractal analysis software Nanoscope IIIa (Digital Instrument Co, Santa Barbara, CA). This software is based on the cube counting method. Basically, a 3-D array of cubes is superimposed on the surface of the 3-D AFM images so that these cubes completely encompass the image [25]. The total surface area at a specific cube size is calculated from the number of the cubes intersecting the surface and the face area of the cubes (cell-area). In this scheme, the size of these cubes was progressively reduced to the predefined cell area or to the pixels of the image. The total surface area is then plotted against the cell area in a log-log scale. For a 3-D fractal analysis, the fractal dimensions (D_s) of these fractured surfaces were obtained from the slope of fractal curve by Eq. (3) as follows:

$$D_s = 2\text{-slope}. \tag{3}$$

It should be pointed out that different fractal analysis methods or different algorithms result in different fractal dimensions. However, results are comparable when using the same software package. The RMS roughness of the surfaces was also calculated from these AFM height images.

RESULTS AND DATA ANALYSES

1. Interfacial Mechanical Properties of Autohesion

The EO copolymers used in this study have different 1-octene content. The characteristic temperatures (T_c) of these EO copolymers were determined from the extrapolation of the plots of the melting point as a function of heating rate to a heating rate of 0°C/min, as shown in Figure 3. These characteristic temperatures are to be used as reference temperatures in the autohesion study, and are 128.4, 123.4, and 122.0°C for EO-1, EO-2, and EO-3, respectively. The characteristic temperatures were used to determine the bonding temperatures which were chosen at 120 and 130°C for the investigation of the bonding temperature effects. Each EO copolymer sample actually was partially or completely melted at these bonding temperatures.

The effects of bonding temperature on the apparent peel strength are shown in Figure 4. Bonding of the EO-1 films cannot be obtained at 120°C, therefore, the T-peel test was not performed. Interfacial failures were observed for EO-2 and EO-3 samples bonded at 120°C. At the lowest peel rate tested, 2 mm/min, the apparent peel strengths

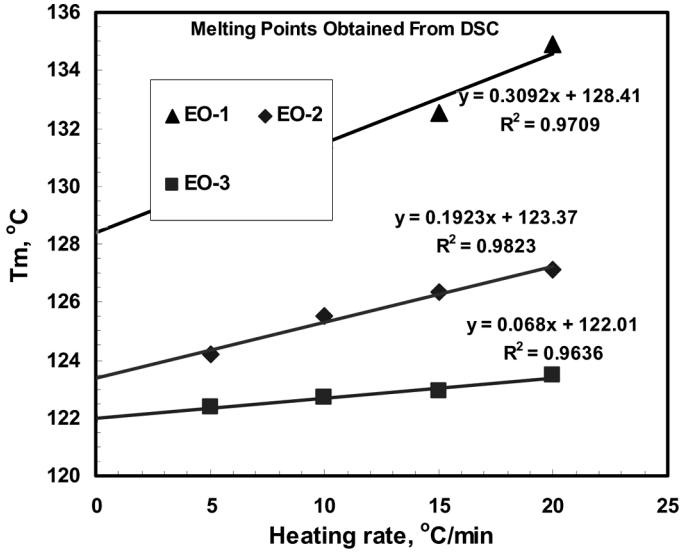

FIGURE 3 Variation of melting temperature *versus* heating rate.

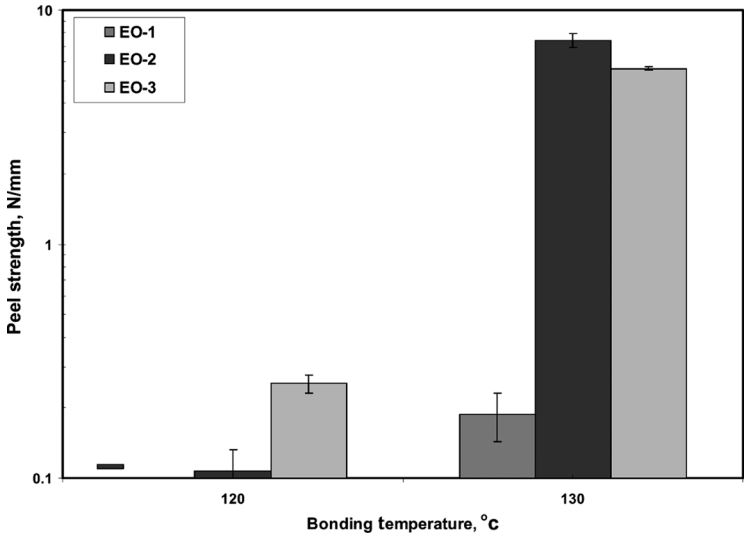

FIGURE 4 The effects of bonding temperature on peel strength for bonded samples at 1 hour. The peel rate is 2 mm/min.

are about 0.11 ± 0.02 N/mm and 0.25 ± 0.02 N/mm for EO-2 and EO-3 samples, respectively. As the bonding temperature was increased to 130°C, interfacial failure was observed for the EO-1 sample and cohesive failure for all the other two samples. The fractal analysis was carried out only on the fractured surfaces resulting from interfacial failures under these conditions.

The peel energies in Figure 5, G_{1C}, are shown as a function of the peel rate for EO-2 and EO-3 samples that have been bonded at 120°C for 60 minutes. For both samples, G_{1C} increases with increasing peel rate. The fracture energy increased from 0.21 ± 0.05 N/mm at 2 mm/min to 0.35 ± 0.06 N/mm at 20 mm/min, and to 0.47 ± 0.01 N/mm at 200 mm/min for EO-2. Fracture energy went up from 0.51 ± 0.05 N/mm at 2 mm/min, to 0.66 ± 0.15 N/mm at 20 mm/min, and to 0.90 ± 0.10 N/mm at 200 mm/min for EO-3. The value of the peel energy of EO-3 is found to be roughly twice that of EO-2 at all three peel rates. It is very interesting that the 1-octene content of the former is also about twice the 1-octene content of the latter. The larger peel energy of EO-3 compared with that of EO-2 could be indirectly due to the higher 1-octene content in EO-3. But it might also be related to the fact that the characteristic temperature of EO-3 is 122°C compared with 123°C for EO-2 which is also a result of different branch content.

Interfacial failures were observed for the EO-1 films bonded at 130°C for 1 hour. Figure 6 shows the peel energy, G_{1C}, as a function of displacement at three peel rates, 2, 20, and 200 mm/min. In the bonding experiments at 130°C, adhesion of the EO-1 films bonded

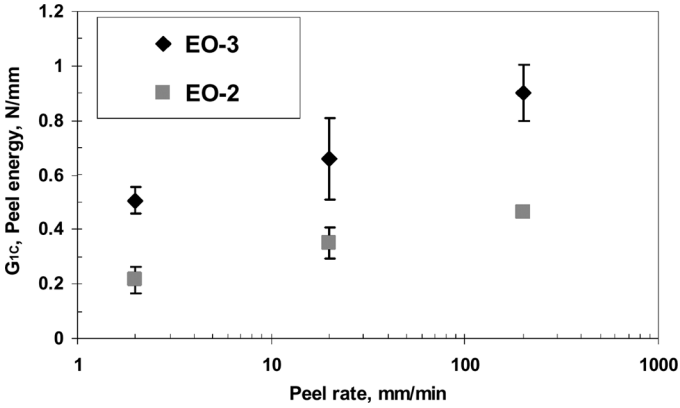

FIGURE 5 The effects of peel rate on peel energy for EO-2 and EO-3 samples that have been bonded at 120°C for 1 hour.

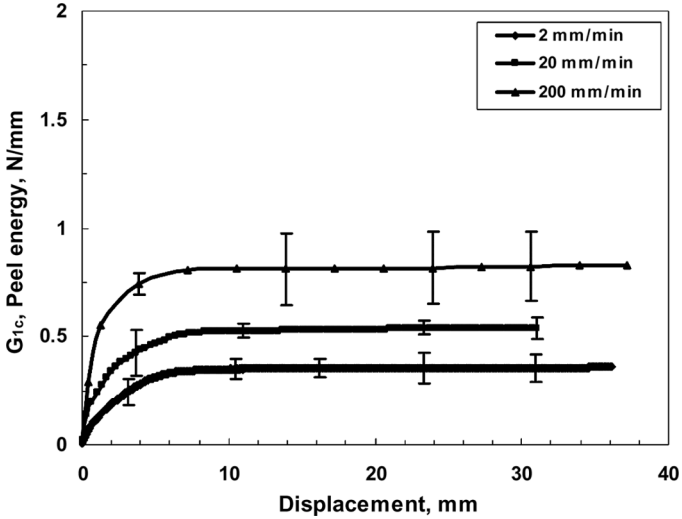

FIGURE 6 The effects of peel rate on peel energy for EO-1 samples that have been bonded at 130°C for 1 hour.

for 1 hour was not good, and resulted in a low apparent peel strength of about 0.19 ± 0.04 N/mm at a low peel rate (2 mm/min) in the T-peel tests. The fracture energy calculated from the peel strength increased from 0.35 ± 0.06 N/mm at 2 mm/min, to 0.55 ± 0.03 N/mm at 20 mm/min, and to 0.80 ± 0.17 N/mm at 200 mm/min.

The peel rate dependence of the peel energy has been discussed in the literature [18,26]. In addition to the energy taken to separate the interface, part of the fracture energy may be attributed to the other deformation modes such as extension and bending of the peel arms, which are sensitive to the change in peel rate. The fractured surface morphology generated from these peel experiments will be discussed later and will provide some information at a microscopic scale in assigning the dissipated energy during T-peel fracture tests.

2. Atomic Force Microscopy (AFM) Images

In order to make comparisons with the morphology and topology of the T-peel fractured surfaces, the surface features of molded films of these four EO copolymers before bonding were examined by AFM. The results are shown in Figure 7. The lamellar structures are apparent on the surfaces. Lamellar structures become more orderly and better defined for the sample with higher 1-octene content. In spite of this

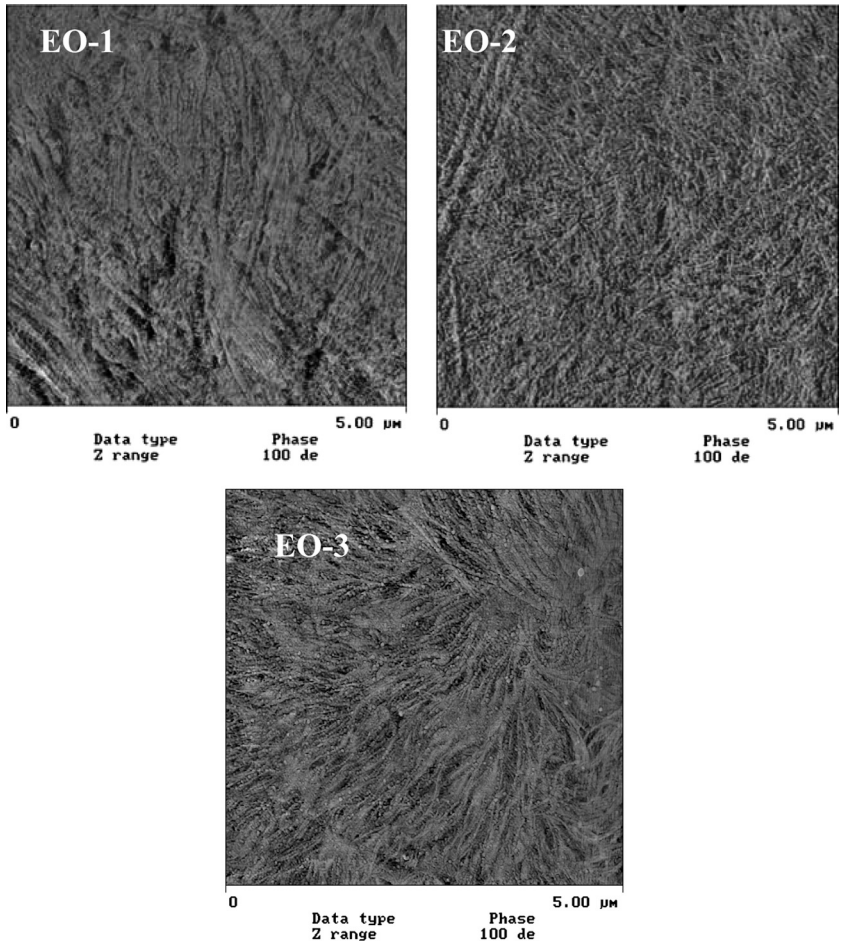

FIGURE 7 AFM phase images ($5 \times 5\,\mu m^2$) of EO samples before bonding.

difference, the RMS roughness of these original (unbonded) films remain at about 4 nm regardless of the scanning surface area, as shown in Figure 8. The value of RMS roughness for each sample is quite similar.

Representative AFM 3-D images and phase images of the original molded film and of the final fractured surfaces of EO-1 samples after the T-peel tests at 2, 20, and 200 mm/min peel rates are shown in Figures 9 and 10. These films were bonded at 130°C for 1 hour. Compared with the surfaces of the original films, much rougher surfaces were observed after welding and the subsequent T-peel fracture tests.

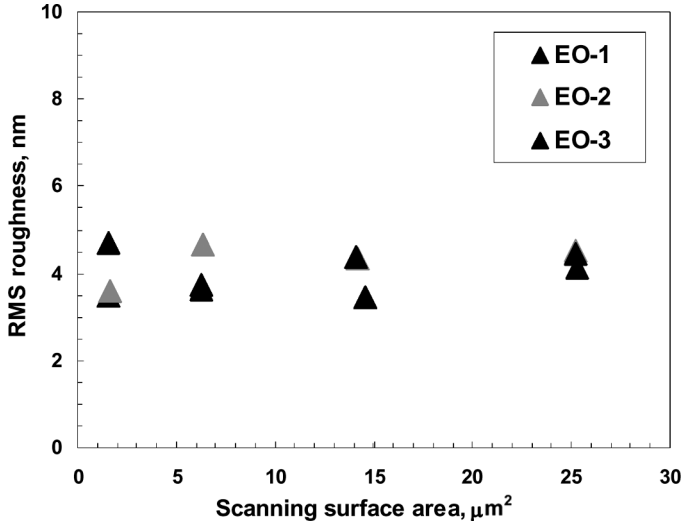

FIGURE 8 RMS of EO samples before bonding.

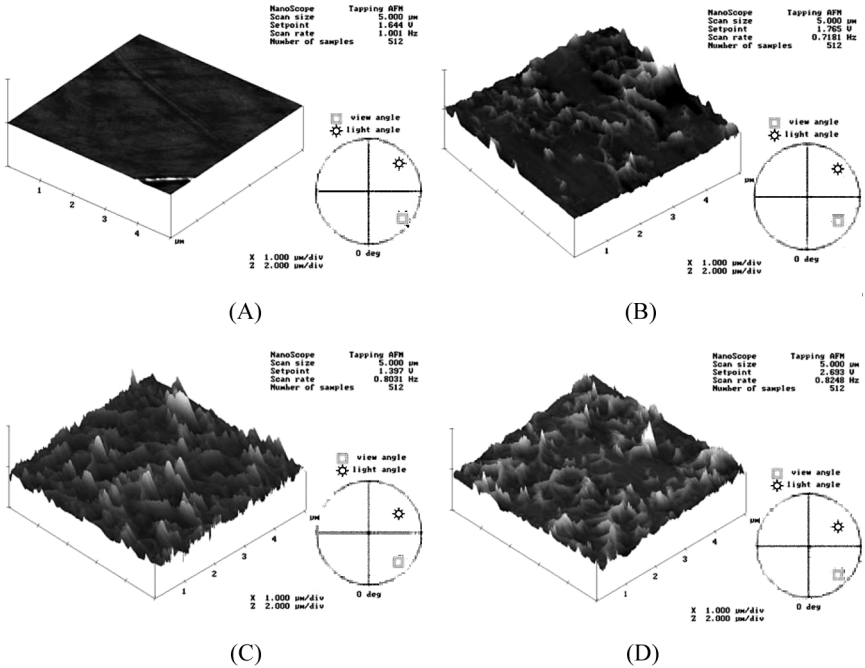

FIGURE 9 AFM images in 3-D of fractured surfaces of EO-1: (A) prebonding; (B) 2 mm/min; (C) 20 mm/min; (D) 200 mm/min.

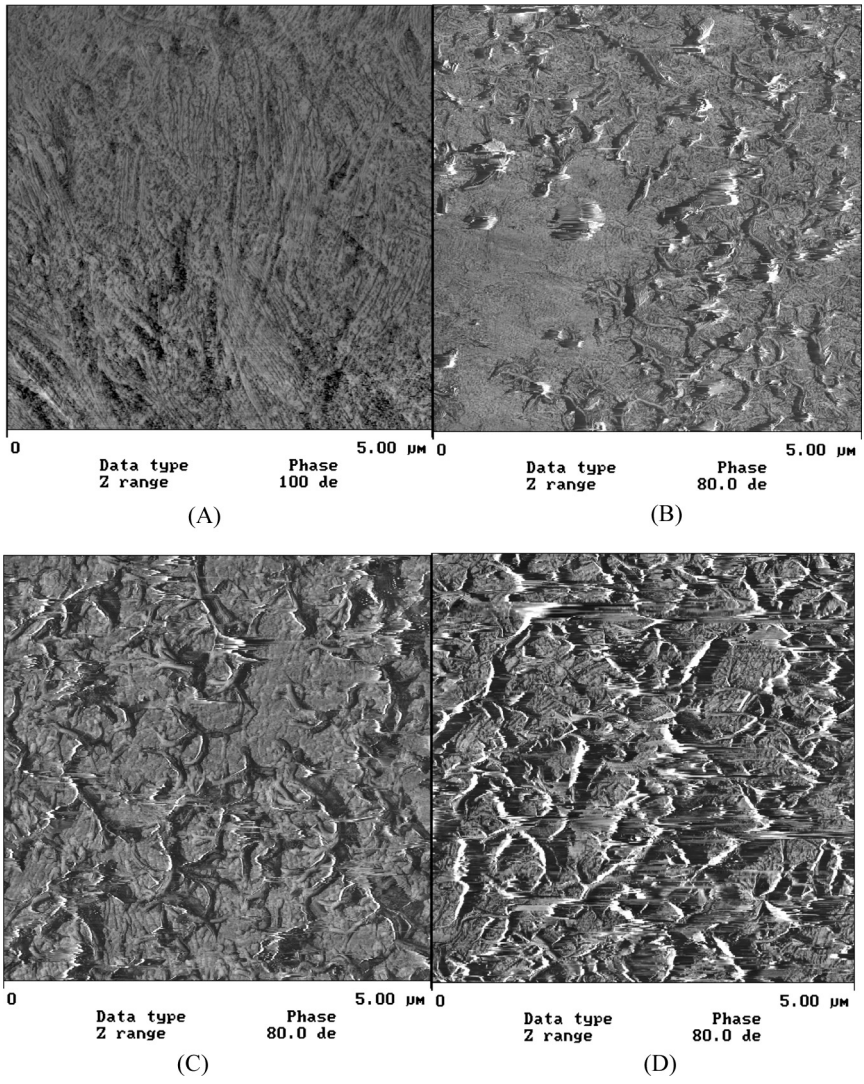

FIGURE 10 AFM phase images ($5 \times 5\,\mu m^2$) of fractured surfaces of EO-1: (A) prebonding; (B) 2 mm/min; (C) 20 mm/min; (D) 200 mm/min.

At the lowest peel rate (2 mm/min), discrete rupture points were observed to have developed on the surfaces. When the peel rate was increased to 20 and 200 mm/min, these rupture points developed into larger, higher fracture surfaces and became more complex. They thus appear more like a network from the AFM phase images. However, it

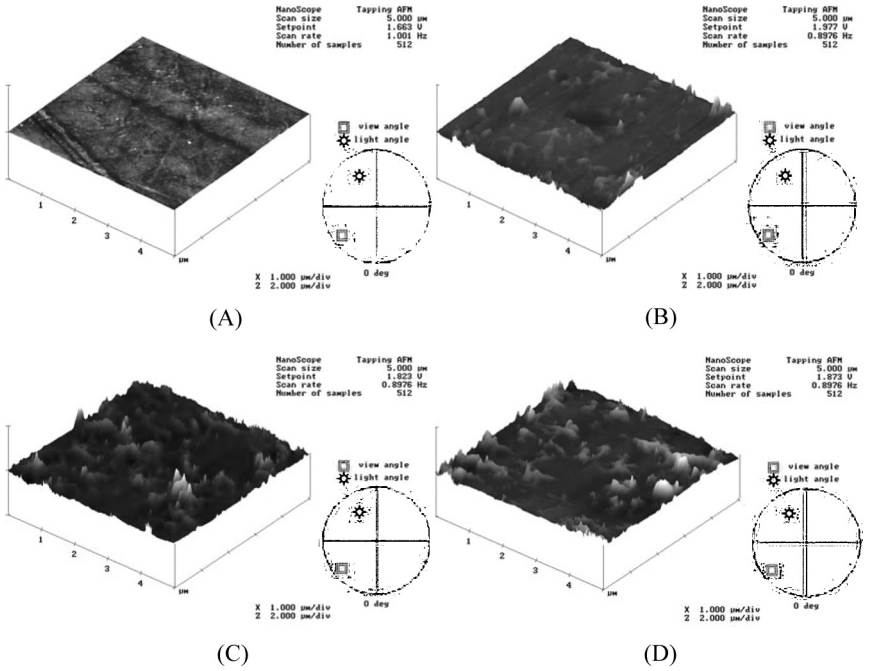

FIGURE 11 AFM images in 3-D of fractured surfaces of EO-2: (A) prebonding; (B) 2 mm/min; (C) 20 mm/min; (D) 200 mm/min.

is difficult to identify any further differences of these images by only visual inspection.

Similarly, the representative AFM 3-D images of the original and the fractured surfaces after the T-peel tests are shown in Figures 11 and 12 for the EO-2 sample. Figures 13 and 14 show the AFM images for the EO-3 sample. These films were bonded at 120°C for 1 hour. EO-2 displayed features very similar to those of EO-1. However, the EO-3 shows some structures with larger size and are less complicated. Further analysis using fractals has been performed on these images in order to provide a systematic and quantitative comparison. This is discussed in the following section.

3. Fractal Analyses on the AFM Images

Generally, when an AFM image of a fractured surface is analyzed by fractal techniques, the upper scale limit typically corresponds to the maximum size of the images, while the lower limit is set by the

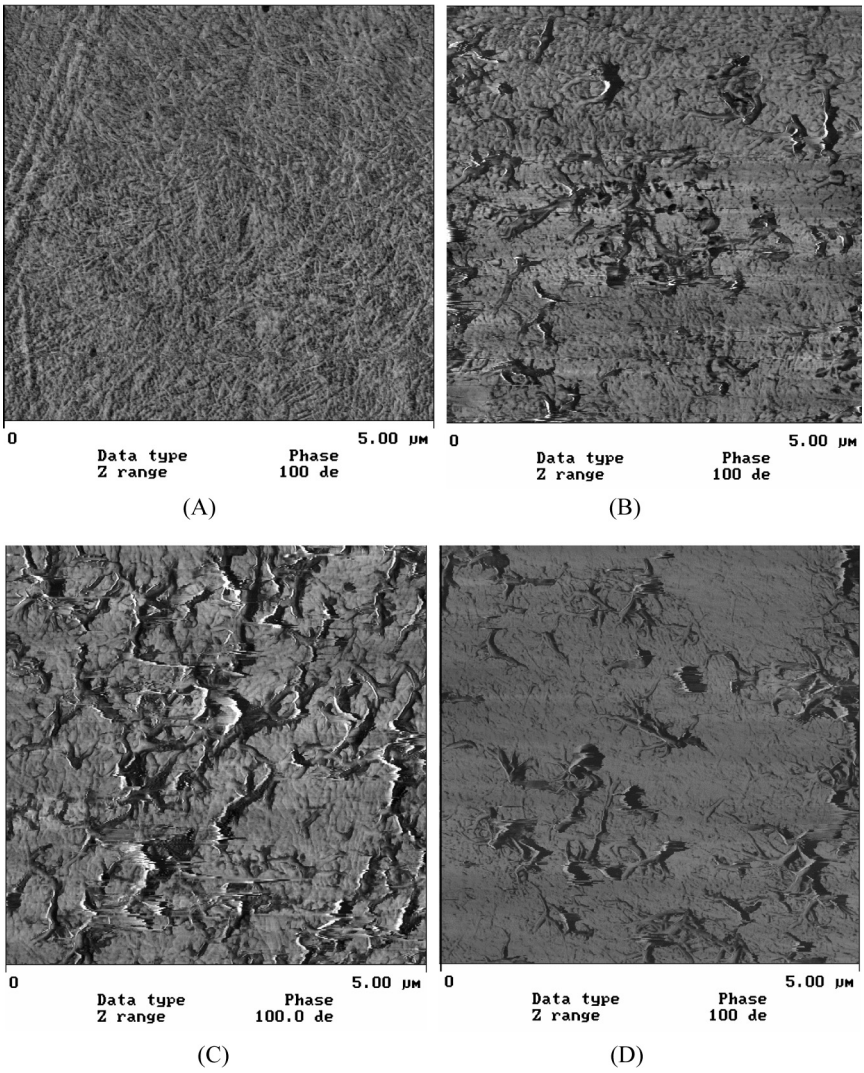

FIGURE 12 AFM phase images of fractured surfaces of EO-2: (A) prebonding; (B) 2 mm/min; (C) 20 mm/min; (D) 200 mm/min.

available image magnification. In the current work, the fractal analyses of all of the AFM images were performed in the scale range from $5\,\mu m \times 5\,\mu m$ to $10\,nm \times 10\,nm$.

Figure 15 shows a comparison of the fractal analysis results of the surfaces of the original films before autohesion for EO-1, EO-2, and

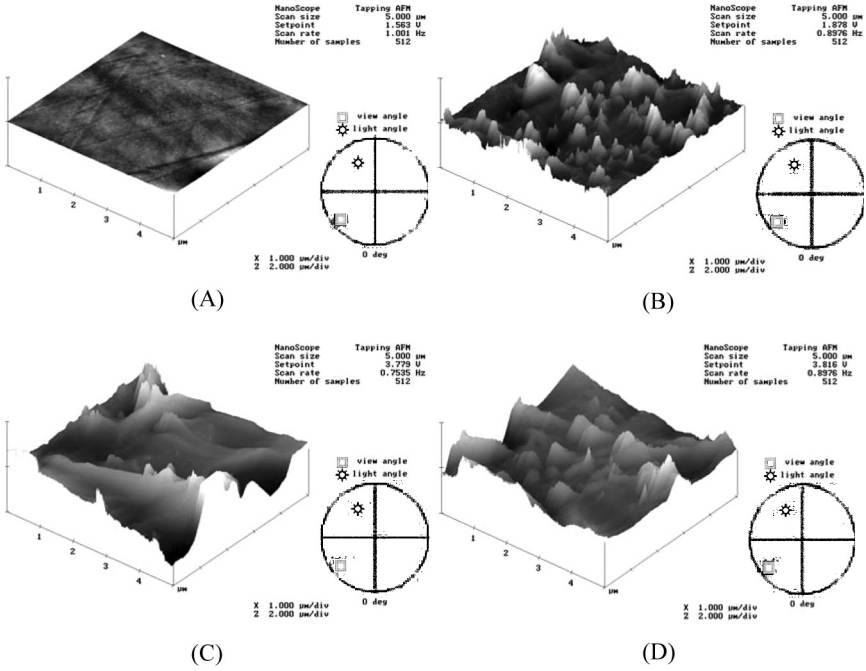

FIGURE 13 AFM images in 3-D of fractured surfaces of EO-3: (A) prebonding; (B) 2 mm/min; (C) 20 mm/min; (D) 200 mm/min.

EO-3. In these curves, the total surface area is plotted against the counting cell area. For all the films, the linear fit through data points could be divided into two distinct regimes, where the slopes are different. The slopes in the first regime are -0.018, -0.094, and -0.081 for EO-1, EO-2, and EO-3 films, respectively. In the second regime which ranges from about $10^{-2}\,\mu m^2$ to the maximum image size at $25\,\mu m^2$, the slope of lines are nearly equal to zero, indicating a "flat" surface at this measurement scale. The cell size that separates these two regimes is defined as the characteristic size of that particular film. Thus, the characteristic sizes of EO-1, EO-2, and EO-3 films were found to be 0.009, 0.016, 0.013, respectively. From a length scale point of view, these characteristic sizes are in the range of 90 to 160 nm, which is about the spacing distance between lamellae as can be seen from both AFM images shown in Figure 7.

A diagram to explain the characteristic size and the schematic surface structures of the molded, pre-bonding films were generated and is shown in Figure 16. The crystal structures are usually

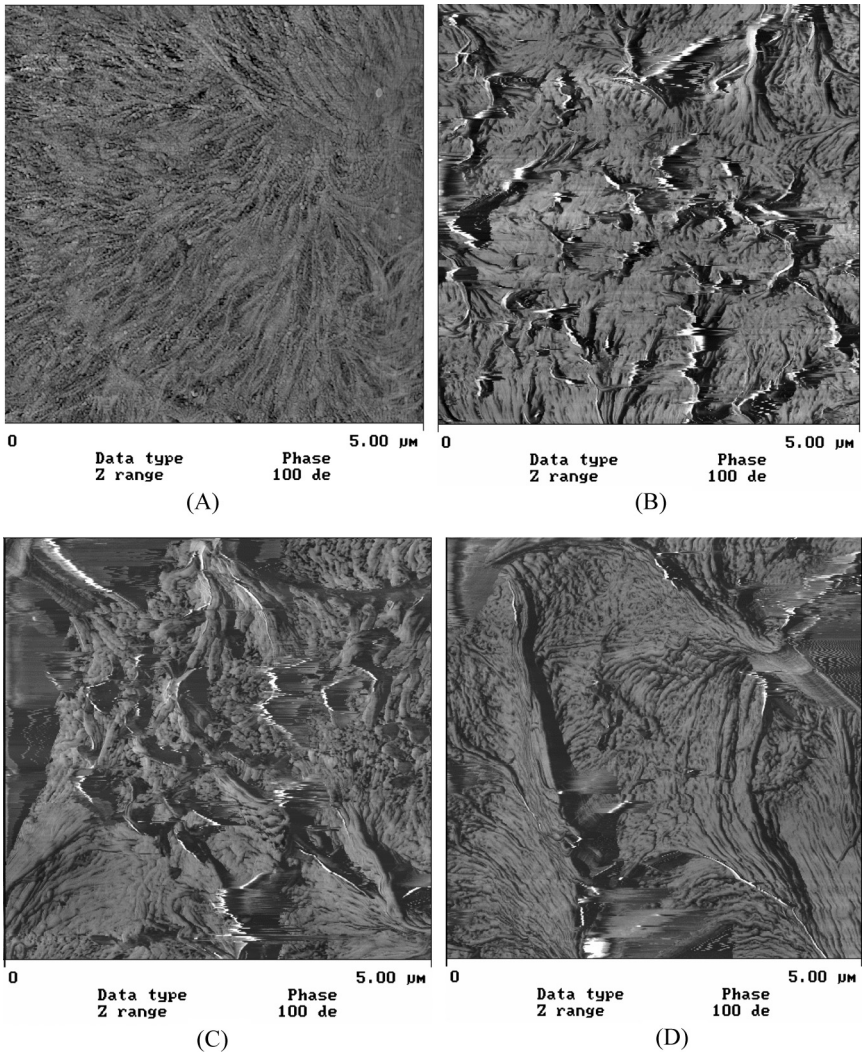

FIGURE 14 AFM phase images of fractured surfaces of EO-3: (A) prebonding; (B) 2 mm/min; (C) 20 mm/min; (D) 200 mm/min.

randomly distributed on such molded surfaces. There are some short chains from the lattice excluded from the surfaces because they cannot crystallize [27]. Typically, the amorphous regions and the crystalline regions appear as different heights under the AFM tip because of their hardness differences. Therefore, when the box counting size from

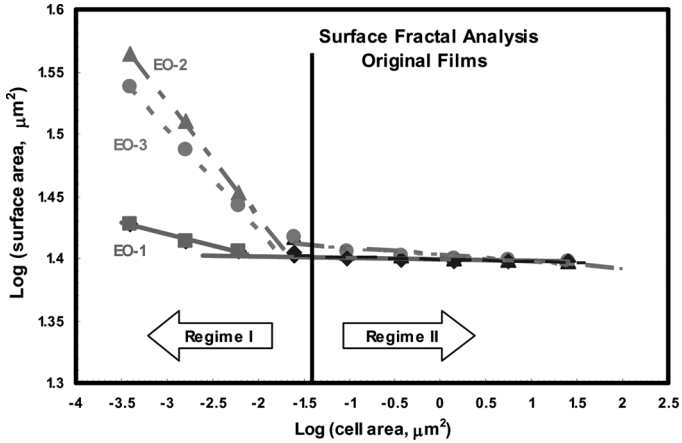

FIGURE 15 Comparison of the fractal analysis (total surface area *versus* counting cell area) of the original EO-1, EO-2, and EO-3 films.

fractal detection is much larger than the size of these crystals, the irregularities inside the crystals and the excluded chains on the surface are insignificant, corresponding to a fractal dimension of very close to 2. However, when the box counting size is quite close to the crystal size, which is of the order of $10^{-2}\,\mu m^2$, a change in the fractal dimension is observed. In the analysis graphs the surfaces are revealed as self-similar on the scale from $0.9 \times 10^{-2}\,\mu m^2$ to 1×10^{-4} for EO-1, $1.6 \times 10^{-2}\,\mu m^2$ to $1 \times 10^{-4}\,\mu m^2$ for EO-2, and $1.3 \times 10^{-2}\,\mu m^2$ to $1 \times 10^{-4}\,\mu m^2$ for EO-3. This is because the local differences between a lamellar and an amorphous layer inside one crystal may dramatically increase the irregularity of these surfaces at the smaller counting scale. At even smaller scales, the excluded chains on the surface would become significant as well.

The fractal dimensions of EO-1, EO-2, and EO-3 samples after T-peel fracture tests are also found in Figures 17, 18, and 19, respectively. Comparing the same regimes of line segments between the original surfaces and the fractured surfaces, the slopes of lines in the first regime have been unaffected, or perhaps slightly increased. However, it is noted that the fractal dimensions in the second regime have increased remarkably. The changes in fractal dimensions and the characteristic cell sizes are tabulated in Tables 2, 3, and 4. These results indicate that the surfaces become more textured after the T-peel fracture tests. As discussed before, the interfacial failures resulted from low adhesion strength of the symmetric bonded joints

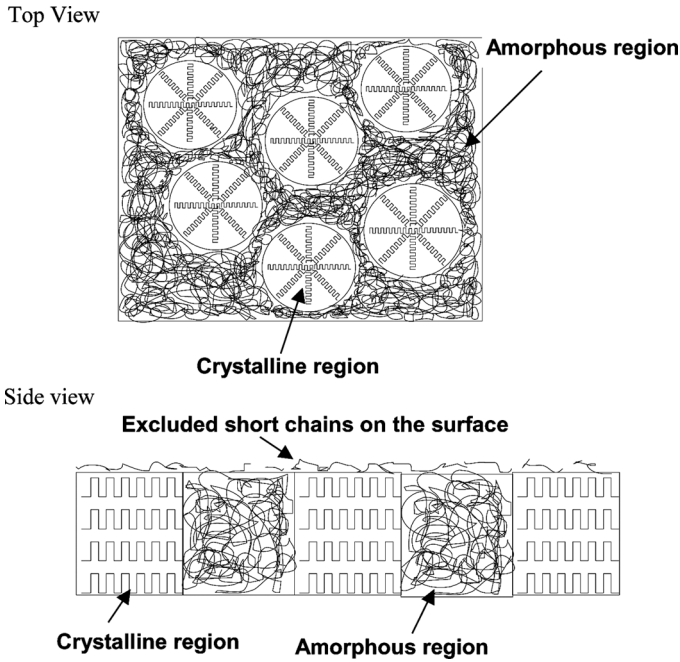

FIGURE 16 Diagram of surfaces features of original films of EO copolymers.

for these three LLDPEs. The small changes in fractal dimensions in the first regime suggest that these low strengths (low available strain energies) are not large enough to deform the underlying lamellar structures. For example, the possibilities for fracture are: 1) the entire crystal structure could be either pulled out as an entity; 2) the crystal structures could be distorted or tilted to some extent due to the interactions between the crystal region and amorphous region; 3) there might be the influence of the movement of the short chains on the surfaces; or 4) chain scission leaves a crystal region unchanged. The small changes in fractal dimensions also indicate that no co-crystallization has occurred between different layers during the adhesion process. Thus, this type of adhesion could be described as a "stitch-welding" in our paper, as depicted in Figure 20. If the bonding temperature is not high enough to let the crystal structure melt in a certain bonding time, only a small portion of the amorphous region and excluded short chains on the surfaces are thought to have inter-diffused in the joining process [28]. These interdiffusion processes will lead to formation of an amorphous interface, which will result in the low bonding strength of

these symmetric EO copolymer interfaces. These described smaller fractal scale events are not major contributors to autohesion.

Even though the fractal dimensions, *D*s, were found not to change with increasing T-peel rate, as indicated from Figures 17, 18, and 19 and also from Tables 2, 3, and 4, the characteristic size did increase monotonically with an increase of peel rate. As mentioned, higher peel energies, G_{1c}, are usually required at higher peel rates due to viscoelasticity. These results indicate that the formation of fractals at the larger scale also corresponds to larger fracture energy. This may be rationalized as the strain energy taken to pull out bigger structures from one side or the other of the bonded interface of autohesion. The correlation between the fractal characteristic size and the peel energy as a function of peel rate also suggests that chain motions inside these interfaces are sensitive to the peel velocity during the fracture process. These may be due to the high chain mobility of these amorphous interfaces when the temperature of the peel tests becomes much higher than the glass transition temperatures of these LLDPEs. Chain entanglements of such amorphous interfaces would, thus, be dominant and lead to the higher fracture energy at the

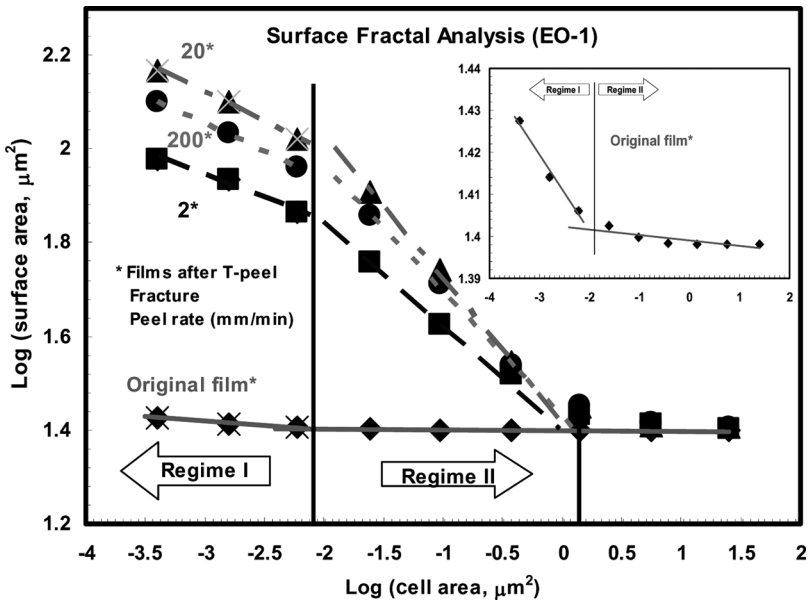

FIGURE 17 Surface fractal diagram of EO-1 before bonding and after T-peel fracture.

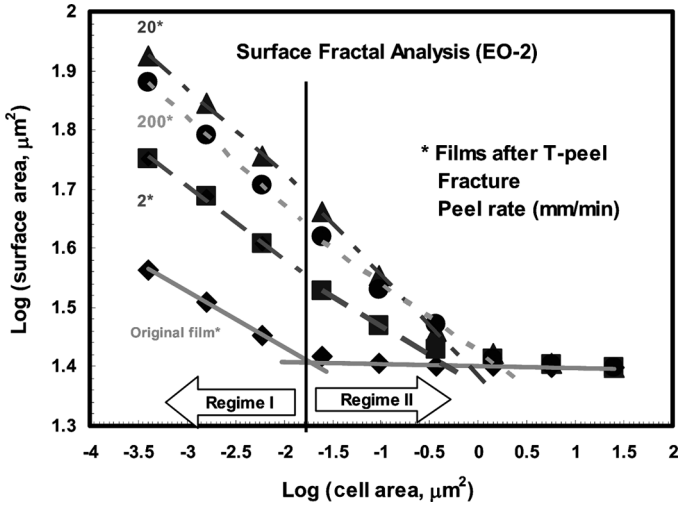

FIGURE 18 Surface fractal diagram of EO-2 before bonding and after T-peel fracture.

higher peel rate. Overall, the larger scale textures created reflect the viscoelastic energy dissipation during interfacial failure for these autohesion bonded EO copolymers.

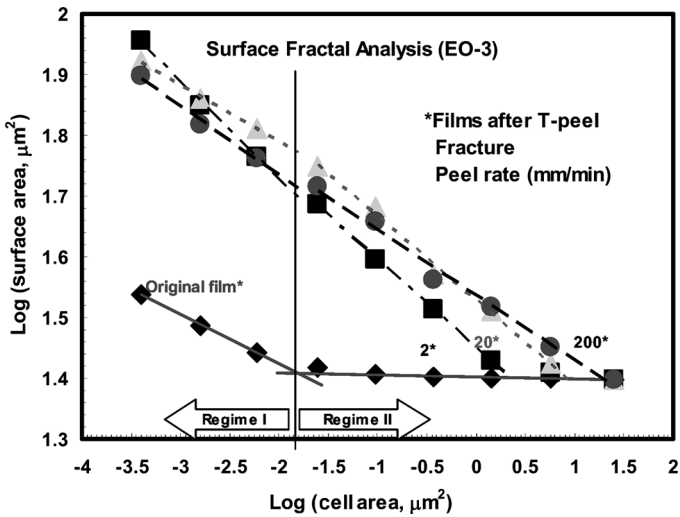

FIGURE 19 Surface fractal diagram of EO-3 before bonding and after T-peel fracture.

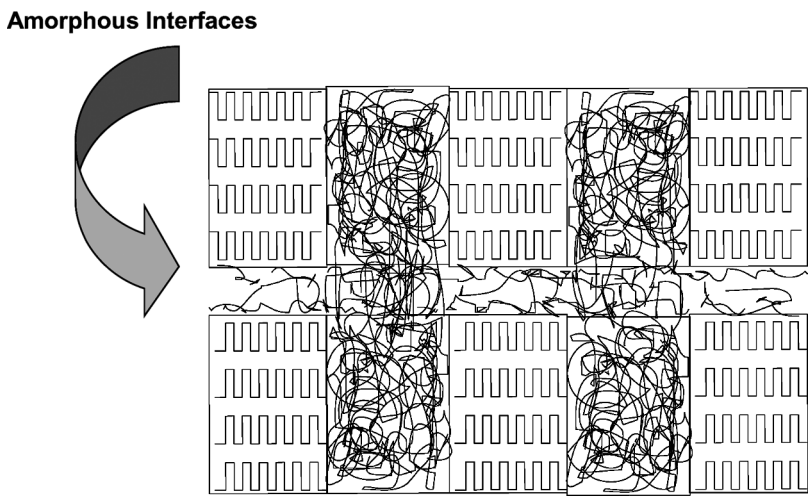

FIGURE 20 Diagram of autohesion process—stitch-welding.

The variations in the fractal dimensions of fractured surfaces among EO-1, EO-2, and EO-3 samples could also be associated with the difference in the properties of the original bulk materials, and in the bonding conditions. EO-1 had the highest crystallinity and density, and was bonded at a higher temperature; these factors made the fractal dimension and characteristic size of the original films and the fractured surfaces different from those of the EO-2 and EO-3 samples.

Chain architecture could be another factor contributing to the differences observed in the fractal characteristic size between the EO-1, EO-2, and EO-3 samples. The autohesion process for EO copolymers has been discussed previously as partially controlled by the chain architectures and the strong effects of the bonding temperatures. Note that, in the present study, the 1-octene content of the EO-3 sample

TABLE 2 Surface Fractal Analysis of EO-1

Peel rate, mm/min	D in Regime I	ΔD in Regime I	D in Regime II	ΔD in Regime II	Characteristic cell size, μm^2
Original film	2.018	0.00	2.001	0.00	0.009
2	2.097	0.079	2.223	0.222	0.857
20	2.123	0.105	2.307	0.306	1.259
200	2.118	0.100	2.269	0.268	1.361

TABLE 3 Surface Fractal Analysis of EO-2

Peel rate, mm/min	D in Regime I	ΔD in Regime I	D in Regime II	ΔD in Regime II	Characteristic cell size, μm^2
Original film	2.094	0.00	2.003	0.00	0.016
2	2.122	0.028	2.101	0.098	0.422
20	2.144	0.050	2.171	0.168	0.794
200	2.146	0.052	2.116	0.113	1.585

is almost twice as large as that of the EO-2 sample; this lowered the melting point of the EO-3 sample more than in the EO-2 case. Further, note the effect of bonding temperature on autohesion which was also considered by investigating the effect of heating rate on the melting temperature of these two EO copolymers using DSC. The characteristic temperature under isothermal conditions was found to be 123.4°C for the EO-2 sample and 122.0°C for the EO-3 sample. The experimental bonding temperature was about 120 ± 0.5°C and that is below the characteristic temperature for both samples. This lower bonding temperature probably produces a lower degree of interdiffusion across the interface because the crystals on the surfaces are almost unmelted, or melted at such a low rate so as to strongly restrict the chain mobility for the interdiffusion process. Consequently, low adhesion strengths were obtained during these T-peel fracture tests. Moreover, the isothermal characteristic temperature of EO-2 is about 1.4°C lower than that of EO-3. Thus, the chain motion of EO-2 will be more confined and, consequently, result in the lower peel energy and smaller fractal characteristic size under the same fracture process.

CONCLUSIONS

The fractured surfaces of EO copolymers were characterized using a cube counting method from fractal analysis of AFM images.

TABLE 4 Surface Fractal Analysis of EO-3

Peel rate, mm/min	D in Regime I	ΔD in Regime I	D in Regime II	ΔD in Regime II	Characteristic cell size, μm^2
Original film	2.081	0.00	2.003	0.00	0.013
2	2.161	0.080	2.145	0.142	2.239
20	2.095	0.014	2.140	0.137	7.943
200	2.115	0.034	2.108	0.105	19.95

Self-similar fractal features were displayed for different finite area scales for all the fractured surfaces. In the fractal analysis of each sample, two distinct regions showing fractal features can be observed in two scale regimes. Fractal features at the smaller length scale (Regime I) were observed at certain conditions for the fractured surfaces and also for the original films. A conclusion is that the fractal features at this smaller featured regime are controlled by the heterogeneous morphology in the surface of these EO copolymers. There were no fractal features observed for the unbonded films at the larger scales (Regime II), only for the fractured surfaces. The fractal dimensions determined in Regime II were computed by using a larger box counting size that yielded a fractal plot comparing the fractured surfaces and the surfaces of original films. It indicated that the characteristic structures of crystals have not been deformed during the T-peel tests. The crystal structures were either moved as an entity or untouched. A stitch-welding model proposed in this article was used to describe the autohesion mechanism; this accounts for low adhesion energies. The fractal dimensions were noted to change slightly with increasing peel rate. The characteristic size at which the fractal features begin to appear increased with peel rate indicating the deformation volume during this fracture test was on a larger scale at the higher peel rate. This observation also provides evidence for the phenomenon of higher peel energy at higher peel rate. Fractal dimensions and characteristic sizes determined from fractal analysis suggest that the fractal characteristics depend on the molecular structures, the processing of the surfaces, and the history of the interfaces. It should be pointed out that different fractal analysis methods or different algorithms result in different fractal dimensions. However, the results are comparable when using the same software package.

ACKNOWLEDGMENTS

The authors thank *Digital* Instruments for discussion of the fractal software. Thanks go to *Dow* Chemical Company for providing the samples. Thanks are also due to the funding support from U.S. Army Research Office/U.S. Army Research Laboratory-funded Macromolecular Architecture for Performance (MAP) Multidisciplinary University Research Initiative (MURI).

REFERENCES

[1] Yang, H., Zhang, W., Moffitt, R. D., and Ward, T. C., *Proceedings of ANTEC 2007*, (Cincinnati, OH, May 6–10, 2007), pp. 1019–1024.

[2] Voyutskii, S. S., *Autohesion and Adhesion of High Polymers* (Interscience, New York, NY, 1963).
[3] Creton, C., *Mechanical Properties of Polymer Interfaces* (John Wiley & Sons Ltd., Chichester, 1999), p. 101.
[4] Wool, R. P., *Polymer Interfaces: Structure and Strength* (Hanser/Gardner Publication Inc., Munich, 1995), p. 65.
[5] Brown, H. R., *Annual Review of Materials Science* **21**, 463–489 (1991).
[6] Russ, J. C., *The Image Processing Handbook* (CRC Press, Boca Raton, 2002), 4th ed., p. 651.
[7] Zhong, Q., Innis, D., Kjoller, K., and Elings, V., *Surface Science Letters* **290**, L688–L692 (1993).
[8] Mendez-Vilas, A., Nuevo, M. J., Gonzalez-Martin, M. L., and Broncano, L. L., *Materials Science Forum* **408–412**, 245–250 (2002).
[9] Marshall, A. G. and Francis, R. V., *Fourier Transforms in NMR, Optical and Mass Spectroscopy: A User's Handbook* (Elsevier, Amsterdam, 1990).
[10] Mandelbrot, B. B., *The Fractal Geometry of Nature* (Freeman, New York, 1982).
[11] Richardson, L. F., *General Systems Yearbook* **6**, 139–187 (1961).
[12] Kunin, B. and Gorelik, M., *Journal of Applied Physics* **70**, 7651 (1990).
[13] Russ, J. C., *Fractal Surfaces* (Plenum Press, New York and London, 1994), p. 29.
[14] Naito, K. and Fujii, T., *International Journal of Adhesion & Adhesives* **15**, 123–130 (1995).
[15] Naito, K. and Fujii, T., *International Journal of Adhesion & Adhesives* **18**, 199–213 (1998).
[16] Whittmann, J. C. and Lotz, B., *Prog. Polym. Sci*. **15**, 909–948 (1990).
[17] Meka, P. and Stehling, F. C., *J. Appl. Polym. Sci*. **51**, 89–103 (1994).
[18] Mueller, C., Capaccio, G., Hiltner, A., and Baer, E., *J. Applied Polymer Sci*. **70**, 2021–2030 (1998).
[19] Kaye, B. H., Image analysis techniques for characterizing fractal structures, in *The Fractal Approach to Heterogeneous Chemistry: Surfaces, Colloids and Polymers*, D. Avnir (Ed.) (John Wiley & Sons Ltd., New York, 1989), pp 55–66.
[20] Pfeifer, P. and Obert, M., *Fractals: Basic Concepts and Terminology, op. cit.,* p. 11.
[21] Stehling, F. C. and Meka, P., *J. Appl. Polym. Sci.* **51**, 105–119 (1994).
[22] Mathot, V. B. F. and Pijper, M. F. J., *J. Thermal Analysis* **28**, (1983).
[23] ASTM D1876-01, Test Method for Peel Resistance of Adhesives (T-peel Test), (Am. Soc. Testing & Materials Philadelphia), **2005**
[24] Xue, Y.-Q., Tervoort, T. A., Rastogi, S., and Lemstra, P. J., *Macromolecules* **33**, 7084–7087 (2000).
[25] Pfeifer, P. and Obert, M., *Fractals: Basic Concepts and Terminology* (John Wiley & Sons, Chichester, 1989), p. 13.
[26] Tsuji, T., Masuoko, M., and Nakao, K., *Adhesion and Adsorption of polymers* (Plenum Press, New York, 1980), Vol. 12A, p. 439.
[27] Pocius, A. V., *Adhesion and Adhesives Technology: An Introduction* (Hanser, Munich, 1997), p. 148.
[28] Brown, H. R., *Scaling in Disordered Materials: Fractal Aspects of Materials: Fractal Structure and Dynamics* (Materials Research society, Pittsburg, 1990). pp 37–38.